Published in final edited form as:
J Neural Eng. 2013 April ; 10(2): 026010. doi:10.1088/1741-2560/10/2/026010.

An Implantable Wireless Neural Interface for Recording Cortical Circuit Dynamics in Moving Primates

David A. Borton[1,*], **Ming Yin**[1,*], **Juan Aceros**[1], and **Arto Nurmikko**[1,2]

[1]Brown University, School of Engineering, Providence, RI 02912 USA

[2]Brown Institute of Brain Science, Brown University, Providence, RI 02912 USA

Abstract

Objective—Neural interface technology suitable for clinical translation has the potential to significantly impact the lives of amputees, spinal cord injury victims, and those living with severe neuromotor disease. Such systems must be chronically safe, durable, and effective.

Approach—We have designed and implemented a neural interface microsystem, housed in a compact, subcutaneous, and hermetically sealed titanium enclosure. The implanted device interfaces the brain with a 510k-approved, 100-element silicon-based MEA via a custom hermetic feedthrough design. Full spectrum neural signals were amplified (0.1Hz to 7.8kHz, ×200 gain) and multiplexed by a custom application specific integrated circuit, digitized, and then packaged for transmission. The neural data (24 Mbps) was transmitted by a wireless data link carried on an frequency shift key modulated signal at 3.2GHz and 3.8GHz to a receiver 1 meter away by design as a point-to-point communication link for human clinical use. The system was powered by an embedded medical grade rechargeable Li-ion battery for 7-hour continuous operation between recharge via an inductive transcutaneous wireless power link at 2MHz.

Main results—Device verification and early validation was performed in both swine and non-human primate freely-moving animal models and showed that the wireless implant was electrically stable, effective in capturing and delivering broadband neural data, and safe for over one year of testing. In addition, we have used the multichannel data from these mobile animal models to demonstrate the ability to decode neural population dynamics associated with motor activity.

Significance—We have developed an implanted wireless broadband neural recording device evaluated in non-human primate and swine. The use of this new implantable neural interface technology can provide insight on how to advance human neuroprostheses beyond the present early clinical trials. Further, such tools enable mobile patient use, have the potential for wider diagnosis of neurological conditions, and will advance brain research.

1. Introduction

Recordings from the mammalian brain with various microelectrode arrays are today widely used to gain access to brain circuits at a high level of spatial and temporal resolution,

*these authors contributed equally to this work
david borton@brown.edu, ming yin@brown.edu, juan aceros@brown.edu, arto nurmikko@brown.edu

Author contributions D.A.B., M.Y., and A.V.N. developed the implantable device platform concept. M.Y. designed the microelectronic circuits and integration of the device. D.A.B. planned, performed, and analyzed data for all experiments with help from M.Y.. J.A. led the manufacturing process and logistics. D.A.B. and A.V.N. wrote the manuscript. A.V.N. led the research project. All authors edited the manuscript.

Competing financial interests The authors declare no competing financial interests.

whereby neural population dynamics can be extracted to develop new computational and functional models of the brain. This is particularly the case for non-human primate animal models which also provide a pivotal translational point for potential clinical applications in the development of assistive and diagnostic neural interfaces. The deployment of intracortical microelectrode arrays (MEA) or sub/epidural electrocorticography (ECoG) arrays as brain sensors [1–3], together with advanced computational neural signal decoding methods, is the subject of wide ranging active research and continues to enrich our understanding of the function of the cortex [4–10]. In addition, animal studies have added much insight into how one must engineer neural sensors to interface with the biology for stable, long term (≫ 1 year) chronic recording [3,11–18].

Current neuroprosthetics research is focused on the goal of enabling people to regain the ability to communicate and control their environment through assistive devices. Recent success in first human clinical trials that take advantage of the single neuron-level recording capability of intracortical microelectrode array (MEA) sensors for access to motor circuits has highlighted how control of a robotic arm or hand by tetraplegic patients is possible [19–22]. Elsewhere, both MEA and ECoG sensors are being studied for the diagnosis and potential early detection of human neurological conditions such as epileptic activity [23,24], showing promise in accessing cortical circuits at spatial resolution not available with EEG-based approaches. Presently, however, these multichannel technologies are percutaneously cabled to electronic instrumentation presenting very relevant clinical risk, are incompatible with mobile subjects, and are restricted in their scalability for larger cortical coverage.

With such human applications in mind, the aim of this paper is to describe a major leap forward in brain-interface neurotechnology by demonstrating a fully implanted, wireless, microelectronic neural data acquisition and telemetry system to replace and reach beyond the current cabled technologies. We demonstrate the neural interface as a high-performance chronic implant in both non-human primate (Rhesus macaque) and swine (Yorkshire and Yucatan) animal models. In our implanted system, the recorded neural signals from the cortex contain the full spectrum of circuit information composed of action potentials, field potentials, and low frequency rhythms from each electrode. The passive intracortical sensor (MEA) is connected to an immediately proximate (<15 cm), head- implanted subcutaneous compact electronic module. The main innovation of this work is the development of the hermetically sealed, chronically implantable, ultra low-power wireless module. A significant neuroengineering point of note is that, in contrast to pacemakers, neural stimulators, and cochlear implants, the amount of continuous data which the 100-channel broadband neural interface must transmit transcutaneously is extremely high. In fact, orders of magnitude higher [16, 25] at 24Mbps (for one 100 element MEA sensor). This very high data rate, along with the simultaneous requirements for very low-power consumption and limited physical volume for circuitry layout make our device unique among those currently developed in the field. The advances we have made to make such a chronic neural interface possible are key achievements of our work and are described in this article.

Development of any implantable active electronic neural interface must be viewed from a holistic perspective to account for the interactions between native and foreign materials, anatomical and physiological constraints, and limitations in size and shape, ease of surgical implantation, and so on. These considerations must be compatible with high performance biomedical device engineering challenges such as neural amplifier performance, signal digitization bit depth, device heat generation, data telemetry, and power sources. Recently, wireless implementation of recording neural interfaces have been seen significant advances in the form of external head-mounted units by exploiting custom microelectronics technologies for acquiring and processing neural data. These systems have been developed in conjunction with percutaneous skull-mounted modules and demonstrated in non-human

primates. [3, 11, 12, 17, 26–31], though none have had the capacity for 100-channel neural broadband operation. Examples of advances at the subsystem microchip electronics level include powerful digital signal processors [17, 32, 33] that feed digitized multichannel neural data to on-board radio-frequency transmitters [12,34,35]. However, none of the head-mounted external-to-the-skin devices has to meet the considerable higher technical and performance demands which we report here to allow the emergence of a first truly implantable, chronically usable, and scalable wireless broadband neural interface. Figure 1 illustrates the performance of our wireless implant in a non-human primate, with raw neural data showing its high complexity and high data content, together with spike (action potential) raster plots and their histograms. The balance of this paper is devoted to the description of the device technology now enabling neural recording capability which, to the best of our knowledge, has not been available to date.

2. Methods

The methods of this paper are broken into two general sections. First, we present a detailed description of the implantable device including design, engineering, and component verification methodologies. Second, we present a description of the validation methodologies including surgical implantation of the wireless implant and in vivo recordings from mobile swine and non-human primates.

2.1. Device design and engineering of the hermetic enclosure

A photograph of the completed 100-channel fully implantable wireless neurosensor device is shown in Figure 2. This device integrates a commercial intracortical silicon based microelectrode array (MEA, Blackrock Microsystems) with a subcutaneous module secured on the skull and below the skin. The 10 × 10 element MEA (100 individual electrodes), much used in the non-human primate community as well as ongoing human clinical trials, had individual electrode impedances ranging from 100 to 800 kΩ (verified by manufacturer at 1kHz), sufficient for single unit isolation [2,36]. The specific neurosensor, including the length of the wirebundle from the MEA to the subcutaneous wireless implant, was chosen to be identical to those employed in ongoing clinical trials [20]. However, due to its unique hermetic high-density feedthough technology, our device allows for a choice of any number of multichannel/multiple site intracortical, subdural, or epidural sensors to be integrated in the future; pioneering work on electrocorticography for neuroprosthetic control from subdural grids [3, 37] inspired our design of neurosensor connector flexibility. For the device in Figure 2, the extracellular neural potentials from 100 cortical sites are fed in to the subcutaneous module. The module, centerpiece of this paper, hosts all active electronics within a 56 mm × 42 mm × 9 mm two-piece Grade 2 titanium alloy enclosure that is hermetically sealed by laser welding. The dimensions of the present device, a balance between size, form factor, and ability to densely pack active electronics into the module, were arrived at by many consultations with practicing clinical functional neurosurgeons.

Multiple key innovations were made when developing the wireless subcutaneous module. First, reaching beyond conventional titanium encased implantable medical devices (e.g. pacemakers), we needed to integrate a brazed single-crystal sapphire window (a diameter of 29.2 mm, greater than $\frac{1}{4}\lambda$ of the data transmission electromagnetic wave to enhance transparency) for electromagnetic transparency that facilitates transcutaneous (i) low loss wireless transmission of RF and/or IR neural data from the device and (ii) inductively coupling wireless power into the device for recharging the embedded battery power supply. The introduction of the sapphire window enables us to eliminate the physical electrical connections for RF or IR data, and RF power between the inside and outside of the titanium enclosure. This reduces safety risks and reliability concerns about routing DC voltages and

currents through feedthroughs. Second, we developed a hermetic feedthrough assembly, resting on the skull, which contains an array of 104 Pt/Ir feedthrough pins embedded in groups of 8 metal-ceramic seals. The layout of this novel high pin-density feedthrough array, whose design had to precisely accommodate local strain during laser welding operations, was designed by our group and manufactured by Cirtec Medical Inc, East Longmeadow, MA. To provide electrical connections from the feedthrough pins to the gold wire bundle from the MEA, a flexible Kapton based interconnect is used (Microconnex, WA), which has a design layout of 100 wirebond pads where the individually insulated 25μm diameter gold wires of the wirebundle are attached (Figure 2d). These wirebond pads are routed using printed traces to gold plated vias that are geometrically aligned with the feedthrough pins at approximately 20 μm fabrication precision. The actual connection from the vias to the feedthrough pins is made with lead-free solder. Among the 104 feedthrough pins, 100 are attached to the MEA through the flexible board and wirebundle, two are connected to 25μm diameter Pt/Ir wires and used as reference electrodes, and the remaining two pins are left open. The feedthroughs and flexible board were overmolded with biocompatible silicone (MED-4211 - NuSil, CA) for protection from the ionically conductive bodily fluids. All microelectronic components including those for neural signal amplification, its multiplexing and digitization, the rechargeable battery and associated circuitry, wireless telemetry, and the battery RF powering circuits were integrated and assembled within the titanium enclosure in a closely packed layered architecture shown in Figure 3. These custom, low power components will be discussed next.

2.2. The guts of the system: microelectronics inside the hermetic enclosure

Current clinical neural data acquisition systems (e.g. BrainGate clinical trials) use numerous electronics outside of the patient to amplify, condition, and digitize the signals from the brain. Our device performs the all of these functions inside the implantable titanium enclosure through the use of custom active electronics (Figure 3). This miniaturization and integration, both functionally and spatially, posed many design challenges which we solved. The overall microelectronic functions are split between two printed circuit boards (PCBs, Figure 4a): the amplification board (AB) shown below the dotted line in Figure 4a, and the radio frequency transmission board (TxB) shown above the dotted line in Figure 4a. We describe the composition and function of each printed circuit board in more detail below.

2.2.1. Amplification Board (AB)—The AB integrates a dedicated preamplifier application specific integrated circuit (ASIC) chip, two successive approximation analog-to-digital converters (SAR-ADCs), a controller ASIC, and a 24MHz crystal oscillator. The preamplifier ASIC consists of 100 low-noise low-power preamplifiers (see [14, 31]) that condition and amplify the incoming neural signals. Each individual preamplifier is a capacitive-feedback, folded cascode operational transconductance amplifier (OTA) configuration with a source follower as the output buffer (Figure 4b). The capacitive-feedback not only sets the gain of the preamplifier to 46 dB, but also creates a low cut off frequency around 0.1 Hz to block the large DC baseline drift caused by the electrode-electrolyte double layer at the input. The high cut off frequency of the preamplifier is set to 7.8 kHz to cover the frequency range of the neural action potential. The entire preamplifier generates 8.6 μVrms input referred noise. During in vivo measurements, the system achieves SNR > 6dB for neural signals > 100μVpp. The 100 preamplifiers are divided into two groups, with 50 preamplifiers each. The outputs of the preamplifiers in each group are multiplexed onto a single analog output and each preamplifier channel is sampled at a rate of 20 kSps. The two multiplexed analog neural signals are buffered with unity gain buffers before they are fed into two 12-bit SAR-ADCs (LTC2366, Linear Technologies). Each ADC running at 1 Msps consumes 4.8 mW from a 3 V power supply and requires a minimum of 14 clock periods for a single conversion cycle initiated by an active LOW chip select signal.

In order to combine the 12-bit effective data from each ADC into a single serial bit data stream to drive the RF and IR transmitters, the multiplexing clocks for the two groups of preamplifiers as well as the ADCs chip select signals are shifted by half an ADC conversion cycle from each other. Thus, the 12 effective bits of each ADC digital output are aligned back to back with no redundant bits (Figure 4a). A controller ASIC we expressly designed for this purpose manages the data flow between the preamplifier ASIC and the ADCs. The digital ASIC injects a 24-bit frame synchronization pattern into the serial digital data stream which is used for demultiplexing, frame-wise error checking, and data recovery at the receiver (described in detail elsewhere [38]). Offline software error checking was also implemented based on the frame synchronization signal. The 100-Channel analog neural signal preamplifier and digital controller were fabricated in a 0.5μm 3M2P standard complementary metaloxide-semiconductor (CMOS) process and measured 5.2 × 4.9 mm^2 and 2 × 2 mm^2 in area, respectively and use a 3 V supply from a low dropout linear regulator [14]. The preamplifier ASIC consumes a total of 6 mW while the controller ASIC consumes 1 mW.

2.2.2. Transmission Board (TxB)—The transmission printed circuit board (TxB) transmits digital data wirelessly from the neural implant to an external receiver which completes the system as a mobile neural interface (Figure 4a). The TxB has 4 connections on a flexible Kapton (DuPont) cable that link it to the AB. Two of the connections are for the 3V VDD and the GND. The other two are for the 24 Mbps serial bit data stream from the AB: First, a TTL stream that modulates a freely running voltage controlled oscillator (VCO), which outputs 5 dBm 3.2 and 3.8 GHz FSK power into a 1.5 dBi low profile (10mm × 10 mm × 0.8 mm) commercial chip antenna (Fractus) for wireless data transfer. The 3.2 and 3.8 GHz FSK frequency is specifically chosen for the minimum interference between commercial wireless devices and our present chronic, proof-of-concept implantable device (we note that our transmitter frequency can be readily adapted to other frequencies in this range, depending on local regulatory demands). Second, an open drain current source that drives an 850nm vertical cavity surface emitting (VCSEL) laser diode for alternative transcutaneous IR data transfer (not employed in experiments reported here, but see [14]). The TxB also houses an inductively coupled wireless charger for a medical grade 200mAh Li-ion rechargeable battery which connects to TxB through a custom flex cable. The wireless charger uses an LC-tank to harvest RF energy at 2MHz from a 40 μH external primary coil driven by a Class-AB power amplifier. The LC-tank consists of 210pF high quality factor (Q) SMD 0603 ceramic capacitor and a coil. The coil is a 27-turn 27 mm O.D. coil made from 46-AWG 40-strand Litz wire for minimum loss (Figure 2b). It has an inductance value of 30 μH with a Q-factor of 75.4 at 2 MHz. The induced AC voltage on the LC-tank is rectified by a full wave rectifier producing a 5V DC supply for a switching mode Li-ion battery charger. The charger IC has >85% efficiency over a wide range of supply voltage (4.35V to 16V) and charging current (0.1A to 2A). The charging current is programmed to be 0.1 A (50% total capacity of the battery) taking 2 hours to fully charge the battery after it is depleted, after which the present version can operate continuously for approximately 6.6 hours. The wireless charger has three safety features: a self-timer that terminates the charging within 2.5 hrs, a battery monitor that indicates the status of the battery, and a protection circuit module (PCM) that protects the battery from over-charging and over-discharging. A low-dropout linear regulator produces 3V supply for the rest of the system from the battery. The inductive power receiving coil, chip RF antenna (ultra-wide band, modulated from 3.28GHz to 3.8GHz FSK), the infrared (IR) semiconductor laser crystal (VCSEL), and battery status indicators were placed directly below the sapphire window for open electromagnetic access. Under implant conditions, the inductive power efficiency of 32% was achieved at a 5 mm distance (with a properly designed external power coil). The RF radio transmitter undergoes < 50% RF loss due to multiple

experimental factors, while we have achieved > 93% IR transparency at a 5 mm distance from the sapphire window. Low-power (mW level) IR is an alternative wireless transcutaneous telemetry pathway described and explored elsewhere [14], but is limited to very short distance data transfer in a transcutaneous application due to scattering by the skin. We employed this transmission modality here for data redundancy and electronic microsystem performance validation.

2.2.3. External Receiving Unit (Rx)—The proper engineering and design of external receiving electronics are largely dictated by the transmitter performance internal to the body. However, several constraints, such as power consumption and space utilization are somewhat more relaxed. We developed portable RF superheterodyne receiver (shown in Figure 4c) for short-range (1 to 3 meters) point-to-point data acquisition from the wireless subcutaneous implant. The receiver uses a 17 dBi planar dual polarized antenna to reduce the sensitivity to movement of the transmitter antenna. The incoming 3.2GHz and 3.8 GHz frequency-shift-keying (FSK) signal is first amplified by a 24 dB low-noise amplifier (LNA) with noise figure (NF) of 0.9 dB, and is down converted to 150 and 450 MHz intermediate frequency (IF) band by a 3.65GHz local oscillator (LO). The IF signal is amplitude-stabilized by an automatic-gain-control block and is then converted to on-off-keying (OOK) IF signal by a 400MHz low pass filter. The OOK-IF is further down-converted to the baseband signal using a mixer and 90MHz low pass filter (LPF). From the baseband signal, the digital data and clock are extracted using a data and clock recovery block. The recovered data is then forwarded to a field-programmablegate-array (FPGA) and repackaged into 16-bit samples, which get buffered though an 8MB SDRAM and sent to a PC via USB 2.0 for further processing and visualization. The sensitivity of the receiver has been measured, both on benchtop as well as two clinical environments, at different received signal strengths, i.e. different receiving distances, using the same transmitter implemented in the implantable device to transmitter a pseudorandom test pattern. The results show that at −77.7dBm input signal strength the receiver bit-error-rate (BER) is 10^{-8} in free-space transmission of 48Mbps. To calculate the BER, first, an 18-bit primitive polynomial linear feedback shifter registers (LFSRs) was used to create a 2^{18} bits long random pattern for testing. This bit stream was sent over the wireless link and received by our custom receiver where is was then compared with the original data to determine the BER.

2.2.4. Modeling heat dissipation of implantable, active microsystems—An issue with any inductively coupled charging system is heat which is inherent to the underlying physics of the process. In case of the wireless implant described here, we have observed a temperature increase during the charging mode of these devices. While the wide aperture sapphire window reduces the heating effect due to induced eddy currents on the surface of the Ti-enclosure, we nonetheless observed a noticeable temperature rise during benchtop measurements. At this stage of the device development we ameliorated this heating by applying active cooling of the skin on all animals in the study. The FDA mandates that a device must meet the ISO 14708-1:2000 E standard requiring no outer surface of a device rise more than $2°C$ above body temperature ($37°C$). We have performed FEM modeling and bench top measurements to characterize heat generation.

As is well known, eddy currents are induced by the time varying magnetic field component of the total electromagnetic exposure. Since the induced currents are quite local and mostly confined to the surface of the conductor, there will be competing currents in opposite directions, yielding an increase in effective resistance of the material due to the skin effect. Given the material properties of Grade-2 Titanium used for the implant enclosure, we calculated a skin depth of 0.257mm at the charging frequency of 2MHz. The titanium shell thickness of the implant, dictated by the brazing and welding required to seal the device, is 1 mm so that eddy current induction will ensue. As a computational model, we created a

COMSOL (multiphysics modeling solution, Stockholm, Sweden) prototype of the current device allowing us to quantitatively estimate the temperature rise of the surrounding tissue given our expected (and measured) power transfer efficiency. These tissues include dermis, skull, and blood vessels. While experimental measurements give us insight into the heating by the subcutaneous implant operation within one set of parameters, it is useful to build a model of the system in order to perturb or adjust variables and obtain expected or predicted changes given various device designs we have made. Thus, we have built a tissue model, based on the work by others [39–42] that integrates our device into a finite element modeled biological environment. This model approximates the bulk tissue in contact with the top and sides of the device as a homogeneous medium and assumes that its boundary temperature remains at body temperature (37°C) during the entire simulation. Titanium has thermal conductivity of 16.4 W/m-°C, heat capacity of 0.523 J/g-°C, and density of 4.51 g/cc. Sapphire, used for the window, has thermal conductivity of 46.06 W/m-°K, heat capacity of 0.799 J/g-°C, and density of 3.98 g/cc. These parameters were used for the COMSOL model, using the bioheat transfer equations. This model assumes a uniform skin tissue with perfusion rate, heat capacity, and thermal conductivity as $6.4e^{-3}$ 1/s, 3600 J/(kg*C), 0.512 W/(m*°C). We model the bone (skull) below the device with the following properties as described elsewhere (Bronzino, 2000).

$$\delta_{ts}\rho C\frac{\partial T}{\partial t}+\nabla\cdot(-k\nabla T)=\rho_b C_b\omega_b(T_b-T)+Q_{met}+Q_{ext} \quad (1)$$

$$T=T_b \quad (2)$$

$$\boldsymbol{n}\cdot(k_1\nabla T_1-k_2\nabla T_2)=0 \quad (3)$$

where δ_{ts} is a time-scaling coefficient; ρ is the tissue density (kg/m^3); C is the tissues specific heat (J/(kg°C)); and k is its thermal conductivity (W/(mC)). On the right side of the equality, ρ_b gives the bloods density (kg/m^3); C_b is the bloods specific heat (J/(kg°C)); ω_b is its perfusion rate (1/s); T_b is the arterial blood temperature (°C); while Q_{met} and Q_{ext} are the heat sources from metabolism and spatial heating, respectively (W/m^3).

We have measured that the charging efficiency is maximized (31%) at 5 mm distance between the primary and secondary coils. During normal charging, 1.4 W power is delivered by the primary coil, 430 mW is received by the device and 970 mW is consumed by the external charging coil, the titanium enclosure, and the internal coil all of which are dissipated as heat. Empirically, we found that of that 1 W, 780 mW was absorbed by the titanium case; the external coil consumed the rest. While temperature increase of the device under constant-charging conditions in air is large ($\Delta T\sim 35°C$; measured experimentally by a thermocouple on the titanium case concurring with COMSOL model in air), in the tissue model the increase was much more modest ($\Delta T\sim 7°C$; calculated from COMSOL model). In vivo, we mitigated heat generation by active cooling. For implanted systems, heat dispersion is mostly accomplished by the natural vascularization of the tissue. For all non-human primates in this study with exposed implants, we actively cooled the microsystem with wet gauze. Cold water was applied periodically during charging to diffuse the heat generated by charging. This type of active cooling was less practical (but used) with an implanted system (in swine); however, it was also less needed as the body has internal mechanisms to cool the tissue, i.e. vessel dilation and tissue perfusion. The COMSOL model of the internally powered microsystem surrounded by skin and bone, as opposed to air, showed modest increases in temperature to the surrounding tissue. The spatial distribution of temperature can be seen in Figure 5 along with the time-varying temperature increase to steady-state. Ongoing research on the next generation of the implantable device in our

laboratory is directed at lowering the heating related effects by combination of eddy current reduction strategies which include changing (lowering) frequency for the charging to well below 1 MHz, and altering the composition of the titanium.

The geometric model used for simulation is shown in Figure 5 along with a generated heat map for the constant charging condition in tissue. Detailed heat generation models like this are crucial to understanding the in vivo impact of implantable, actively powered microsystems. We have used this model not only to evaluate the temperature increase of our device and the surrounding tissue, but also to give insight into modifications for future power transmission methodologies.

2.3. Surgical procedures for Wireless Implant

Specific surgical procedures were developed to implant the wireless neural interface into the swine and non-human primates. All procedures were approved by the Brown University Institutional Animal Care and Use Committee under the protocol #0911091 and performed by (or supervised by) a trained clinical neurosurgeon. Two Yorkshire swine (SA, SU) were implanted with a device. Animals were induced with a Telazol (4 mg/kg) / Xylazine (2 mg/kg) mix injected intramuscularly. Swine were then intubated and maintained on Isoflurane (1.4% MAC) with constant IV delivery of lactated Ringers solution (130 mmol/L of Na^+, 4 mmol/L of K^+, 3 mmol/L of Ca^{2+}, and 109 mmol of Cl^-). Once transferred to the operating table, a custom stereotactic frame for large animals was used to secure the cranium for the duration of the surgery [15]. Under sterile conditions, an arced incision was made to minimize pressure on the implant. The incision began on the left caudal aspect of the dermis, continued rostral then returned caudally to the right aspect of the dermis and finally was reflected. The periosteum was then reflected and sometimes incised for use as a dural supplement. A cavity was made centered on midline and roughly 5 mm deep with a Stryker cranial burr to accommodate the device. Once the cavity had been made to the geometry desired, a small (15mm × 20mm: AP × ML) craniotomy was created with a craniotome (Stryker) for access to the brain. The dura mater was incised and reflected, exposing the upper rostrum area of the primary somatosensory cortex. An Ethylene-Oxide sterilized device was removed from its packaging (custom designed sterilization and transport case) and placed in the surgical field. The attached microelectrode array (Blackrock Microsystems) was then placed on the target cortical location and inserted 1.5 mm through the arachnoid and pia mater into cortex with a pneumatic drive (Blackrock Microsystem) at 172 kPa. Once insertion was confirmed, the dura mater was re-approximated above the MEA and sutured (6-0 silk) to form a near-water-tight seal. Surgi-Cel was placed in the craniotomy to help seal the dura and fill the void left from the craniotomy. The remaining portion of the device was then placed in the cavity previously formed and 5 titanium screws were used to fix it to the cranium. Finally, the surgical site was flushed with Bactrim (trimethoprim and sulfamethoxazole) and the dermis was sutured closed over the device (3-0 vicryl). It should be noted that the device was fully functioning and operating during the entire implantation process, a potential scientific and clinical monitoring advantage to wireless neural interfaces. A Fentanyl patch (2 μg/kg/hr) was used to manage postoperative pain. In swine, the wireless device was implanted in the primary somatosensory cortex based on functional atlases [43–45].

After validation in swine, two devices were then implanted in two rhesus macaque non-human primates (JR and JN, 8.6 kg and 5.9 kg, respectively). The surgical approach used procedures very similar to the swine implantation. Animals were induced in their home cage by an intramuscular bolus of Ketamine (15 mg/kg) for safe transport to the operating room. IV access was gained on the femoral vein for delivery of fluids. The animals was then intubated and maintained on Isoflurane (1.4 to 1.6% MAC) for the remainder of the case. A midline skin incision was made and the dermis was then retracted along with temporalis to

expose the cranium. A craniotomy was then made (20mm × 17mm: AP, ML) with a craniotome (Stryker) exposing the intracranial space. The dura mater was incised and reflected over the arm area of primary motor cortex (MI), our target implantation region. An Ethylene-Oxide sterilized device was removed from its packaging and placed in the surgical field. The attached microelectrode array (Blackrock Microsystems) was then placed on the target cortical location and inserted 1.5mm through the arachnoid and pia mater into cortex with a pneumatic drive (Blackrock Microsystem) at 172 kPa. Once insertion was confirmed, the dura mater was re-approximated above the MEA and sutured (6-0 silk) to form a near-water-tight seal save the wirebundle protrusion. The bone-flap from the craniotomy was repositioned and secured onto the cranium with titanium craniomaxillofacial strips (Stryker) to protect the cortex from polymethyl methacrylate during the positioning process of the device. The casing of the device was then secured to the cranium with 5 titanium bone screws (Stryker). Non-human primates have significantly smaller skulls than humans as well as a significantly thinner dermis. For this reason, and as JR and JN (JN specifically) were relatively small monkeys, closure of dermis would have been physically difficult. Thus, we decided not to close the dermis so as to prevent subsequent problems and potentially compromising the superficial vasculature and skin integrity in these first implant experiments, whose goal was to validate and exploit the chronic use of the device in monkeys. With larger macaques, we expect that full closure of the dermis can be implemented without complications and are currently pursuing such experiments yielding positive results. In JR and JN, clinical grade PMMA (Stryker) was used to fill voids underneath the device from the extreme curvature of the skull and to provide a flat solid platform for the case to rest on (similar to the shaving of the skull for the swine implant); hence the case was left partially exposed. Specifically, the MEA, wirebundle, and feedthrough assembly were embedded in tissue, while the majority of the titanium can was embedded in Polymethyl-methacrylate (PMMA). The monkeys JR and JN have had no need of any subsequent surgical intervention thus far during the twelve months post implant. We note that preliminary results in large non-human primates and early guidance from experienced neurosurgical colleagues make us confident that the device is safely implantable subcutaneously in human subjects in its present implementation, as it was here in swine. the devices were tested to verify electronic function in the operating room immediately before and after implantation into cortex. In monkey, devices were implanted in the hand area of the left primary motor cortex with wireless recordings reported below.

We note that the swine device implantations represent the subcutaneous and chronic scenarios since all components of the devices were immersed in body tissue. The NHP implants, while functional when implanted chronically, were only partially subcutaneous. For anatomical comparison, and focusing on the placement and size of the subcutaneous titanium electronic module, Figure 6 shows X-Ray images taken from the implants from a swine and a rhesus monkey after several months of implant. The present form factor was decided jointly in consultation with neurosurgeons, with a view towards human clinical translation. Interestingly, while no (obvious) neural modulation could be seen immediately following device implantation during the surgery (device can be operated sterile), recordings of single unit activity were present in data collected just two hours post implantation as the animal was returned to its home cage for surgical recovery. These devices in non-human primates recorded single unit activity on over 70 input channels; several channels showed multiple single unit activity. These numbers compare well with the neural population recordings with MEA implants by the cabled version of the Blackrock Microsystems NeuroPort in humans [20].

2.4. Wireless System Operation: Animals in Home Cages

On days of recording, pigs were sedated with Dexmedetomidine for initial charging of the fully implanted system. A pulse-oxymetry monitor was used to ensure effective oxygen perfusion was maintained during the sedation period since Dexmedetomidine is a respiratory depressant. The external charging system was placed near the skin (<5 mm) above the implant and turned on for 30 minutes, allowing for one hour of operation. Pig skin is very thick (1cm), reducing the efficiency of inductive coupling and transfer of power to the battery. Much of the forward power at this distance is reflected back to the primary coil and is dissipated as heat at the primary coil. A small portion is also absorbed by the tissue itself. Since heat from the primary coil can reach the skin through convection, the tissue itself is absorbing RF power dissipated as heat, and the skin effect on the Ti casing, we actively cooled the skin with cold saline to maintain a comfortable temperature for the animals. After recharge, the device immediately turns on and the sedation agent was reversed with Atipamezole. The pig was then free to roam around its home cage while neural recordings were collected over the wireless link from the implanted microsystem. Devices in two pigs were charged and recorded from once per week for the first month, then variably over the next 12 months - a period of >380 subject days (limited by the animals physical growth from initial 40 Kg to well over 100 Kg).

Non-human primates, after complete recovery from surgery, were sedated with a light dose of Ketamine (5 to 7 mg/kg), removed from home cage, and placed on a table charging the device. The external charging system was placed near the device (< 3 mm) above the implant and charged the system for 30 minutes. Charging currents of 80 mA were expected from bench top measurements. We did not incorporate a means to measure charging current on implanted devices and plan to add this in future versions. As one measure of battery health, we observed a consistent charge-time to run-time ratio over the complete study of over one year. After 30 minutes of charging, the animal was placed back in its home cage and watched until completely recovered from sedation. Once recovered, neural data was collected wirelessly for 1.5 to 2 hours via a receiving antenna placed on the outside of the home cage. Video footage was collected and time-locked with the neural data defining states of monkey behavior, e.g. reaching for an apple, scratching head, or turning head. All behavioral events were labeled offline and synced with the neural data in Matlab to produce plots shown in Figure 7. In both swine and non-human primates, recording sessions were terminated when the battery reached the turnoff point set by the charge controller.

For analysis of freely moving, wirelessly collected data, we turned to recent work in single-trial “neural trajectory” analysis [8]. Neural trajectories are a low-dimensional representation a system as it evolves through time and a useful tool to analyze dynamical neural states. In addition, such methodologies aim to expose common underlying structure to the information content, and neural network, of the cortical area from which we are recording. To create such trajectories, raw (broadband, 20ksps) binary (12-bit samples from the ADC) data encoding voltage values on each input microelectrode were first filtered with a 500 to 5000 Hz finite impulse response (FIR) bandpass filter. Spike extraction was performed by an implementation of the multiresolution Teager energy operator [46], applied here to the filtered input on each electrode to obtain action potential peak indices in the recording. The extracted action potentials were then binned every 100 ms and smoothed with a Gaussian kernel yielding the smoothed firing rate on each channel. Principal component analysis was then used to align the smoothed firing rate of each input channel by contribution to the variance in the signal. Many other decomposition algorithms could have been used, such as the recently explored Gaussian Process Factor Analysis [47]. When observed dynamically over time, the evolution of the first two or three principal components over time is often termed the “neural trajectory”. Here, we they were used to describe the dynamic state changes of the cortical network. This method of analysis is well documented elsewhere [8,

47, 48]. We present neural trajectories produced during free movement of monkey JR: scratching eye (blue), touching an apple (green) and turning head (purple) in Figure 7.

3. Results and Discussion

We have presented a novel implantable neural interface capable of broadband recording seen in Figure 1 over a high speed wireless connection. The present, first version of the completely implantable system consumes 90.6 mW during normal operation while transmitting at data rate of 24 Mbps over a distance of > 1 m. The final neural interface weighs a total of 44.5g, 7.4g of which are from the battery, 30.6g from the Titanium packaging, and the remaining 6.5g constitute the PCBs and electronic components. The architecture of, and method for, integration of the above mentioned electronics into an implantable, hermetic package represents in our view a unique device development for broadband neural interface applications. A focus on ultra-low power circuitry and efficient radio telemetry enable the neural interface to be operated continuously across all 100 channels for 7 hours on a single charge cycle; an engineering solution for up to 16 hours of operation is currently being developed by our group - rationally compatible from a health care provider point of view such as one hospital shift. The detailed performance of our implantable device is shown in Table 1 along with other state-of-the-art recording systems as a comparison. It should be noted that very few systems have been implanted to fully validate their performance - a critical step proving clinical readiness.

The full electronic functionality of the manufactured wireless neural recording system was verified on the bench (5 units) to assure battery performance, amplifier accuracy, and data telemetry were completely functional. After the surgical implantation of the neural interface into swine and monkey animal models we proceeded to evaluate the performance of the wireless neural interface through data collection and analysis. Two swine [15] were first implanted for initial system validation and chronic testing and recordings were made while animals foraged in their home cage. In addition, the two rhesus macaque non-human primates (JN, JR) were implanted to explore the neuroscientific utility of the neural interface and future potential clinical use. We have operated individual devices chronically for periods exceeding 12 months in swine and non-human primate models (swine: SA = 3, SU = 13 months; macaques: JR = 14, JN = 13 months) without any noticeable electronic performance degradation or impairment (experiments ongoing). It should be noted that recording fidelity (i.e. number of electrodes displaying clear single-unit activity) has diminished over time, consistent with the literature on Blackrock MEA recording longevity and discussion of such mechanisms is out of the purview of this paper.

The devices in animals SA and SU showed clear neural spiking activity with peak-to-peak amplitudes 40 to 250 μV, day-in and day-out. Recordings were made over 2 months from animals in their home cages with the RF antenna, receiver, and ×86 PC laptop immediately outside the cages (after this time the animals had usually outgrown in size their holding area). In both swine and monkey experiments to date, no electronic leakage whatsoever has been detected to suggest a compromise in the hermeticity of the titanium case. Devices were helium leak tested at fabrication as per medical standards for comparable Ti-enclosures which, while endowed with much fewer feedthrough connections than our custom device, are generally used in applications requiring two or more decades of reliability. Likewise no crosstalk has been observed on the input wiring from the intracortical MEA, pointing to good electrical isolation of the feedthrough pins. In the two non-human primates (JR and JN) the devices each recorded consistently single unit activity (along with local field potentials) on over 70 of 100 input channels; several inputs showed multiple single unit activity (Figure 7b). While unit counts as expected dropped over time (12 recording sessions over 13 months for longest case in swine, 15 recording sessions over 14 months per non-

human primate), this level of performance compares well with the percutaneous electronics-outside-subject system deployed in recent human clinical trials [19, 20, 52–54] and are likewise comparable to those reported in the numerous monkey publications [6,55–60].

During typical recording sessions, the amplifier output on all channels showed consistent input referred noise level of $8\mu V_{RMS}$. These values are in agreement with the expected performance based on circuit simulation of the employed amplifier ASIC technology and have been subsequently reduced to $3.2\mu V_{RMS}$ in later chip revisions currently awaiting device integration [61]. We emphasize that the entire microelectronic device design represents a judicious optimization between performance and power consumption in a broadband implantable neural interface. Power consumption and considerations for heat generation also arise during inductively coupled battery charging, as noted by others [26]. In this first implementation of an implantable neural interface, we expected (from discussed modeling) a $7°C$ increase in system temperature and we observed an increase in skin temperature above the device. While skin temperature may only increase by $2°C$, this does not mean the internal tissue is not increasing more, as in fact our models would predict. The system has not been optimized for heat management and must be addressed in future hardware engineering. As a temporary solution, heating during charging was mitigated by liquid cooling the area with chilled water during the recharge process and did not noticeably affect the animals comfort. During normal operation (not charging) no significant heating was expected from the device as internal electronics consume only 90.6 mW and any heat generated would be distributed over a large area. If we assume $1°C$ for 20mW/cm^2, and we produce 100mW/23cm^2, this leads to about a $0.26°C$ increase due to the operation of the device.

Data was successfully transmitted from the neural interface at 24 Mbps a distance of approximately 1 meter during experiments to the receiving antenna, outside the animals home cages. Figure 7 summarizes characteristic data acquired from one of the monkeys (JR), while in his home cage during normal spontaneous behavior activity (including scratching his head, reaching for a treat, and other natural movements). Both spike trains and local field potentials were recorded wirelessly during several months of testing. Transmitting radio frequency information from within a metal cage is a challenging problem. Wave reflection from the cage can attenuate the signal due to interaction of multiple paths from the transmitter to the receiver. We have designed an antenna and receiver combination to reduce the errors in the telemetric link [61], however, this solution is not perfect. We are currently working on receiver designs to reduce multipath issues, potentially leveraging multi-in-multi-out (MIMO) architecture. Data recorded during freely-moving sessions, such as that shown in Figure 7, give us confidence that this wireless neural interface will enable future research on primate natural behavior. We have used the spike data to interpret and differentiate the particular movements associated with animals natural behavior by projecting the multidimensional spike train data onto a two-dimensional representation of neural trajectories (Figure 7f). The ability to record natural movements from a distance without disturbing the subject brings with it the potential for new insights into the subtleties of motor dynamics and into the cortical pathways controlling movement.

In summary, we have reported on the development of a new wireless, chronically implantable neural interface technology, enabling broadband recordings to be made by an implant over a high-speed radio-frequency link in untethered animals. The work is pertinent to the next generation of neural prostheses for severely neurologically impaired human patients with the final goal of endowing them with significantly increased mobility and wireless access to assistive device technologies. As a proof of device performance and viability, the neural interface was implanted in the primary somatosensory cortex (SI) of two Yorkshire swine and the primary motor cortex (MI) of two rhesus macaque primates. In

swine, 100 input channels of broadband neural data were recorded during spontaneous activity and used for device verification and validation over 13 months combined. In primates, 100 input channels containing neural data were simultaneously recorded over 27 months combined. In addition, broadband neural data was collected outside the animals' home cages, enabling analysis for reconstruction of motor cortical neural state trajectories during specific naturalistic movements. Moreover, this early mobile collection of neural data prompts the question of how to build future behavioral tasks to elucidate currently not-understood dynamics of the cortex. The high fidelity recording of both spikes and local field potentials suggest that the implantable device can enrich fundamental brain science in primates under naturalistic, freely moving conditions. Our introduction of a wireless interface capable of untethered broadband neural data collection beckons use in other clinical diagnostic applications such as epilepsy monitoring where, currently, patients are tethered to the bedside during neurological assessment.

Acknowledgments

We thank John P. Donoghue for his neuroscientific guidance and collaborative role in this project. In addition, we acknowledge the roles of Cirtec Medical Inc, Microconnex Inc, CV Inc, and Blackrock Microsystems Inc, in their important role for fabricating specific components of the implantable device. We thank Drs. James Barrese, Sydney Cash, Leigh Hochberg, and Moses Goddard, for their surgical and neurological expertise. We acknowledge Kineteks Inc for fabricating the sterilizable and ESD-proof holder for devices through a constructive collaboration. Many members of the Brown University Neuroengineering Laboratory made key contributions: we especially thank William Patterson, Christopher Bull, and Naubahar Agha. The expertise and dedication of the staff of the Brown University Animal Care Facility was invaluable, and we thank Dr, James Harper, Veronica Budz, Roxanne Burrill, and Pamela Norberg. All animal experiments were conducted according to Institutional Animal Care and Use Committee guidelines and the USDA under protocol #0911091. This work was supported in part by the National Institute of Health (NIBIB and NCMRR/NICHD, 1R01EB007401-01), the National Science Foundation under the EFRI Program (#0937848), and the DARPA Repair Program (Contract N66001-10-C-2010).

References

[1]. Jones, Kelly E.; Campbell, Patrick K.; Normann, Richard A. A glass/silicon composite intracortical electrode array. Annals of biomedical engineering. Jul; 1992 20(4):423–437. [PubMed: 1510294]

[2]. Nordhausen, Craig T.; Maynard, Edwin M.; Normann, Richard A. Single unit recording capabilities of a 100 microelectrode array. Brain Research. Jul; 1996 726(1-2):129–140. [PubMed: 8836553]

[3]. Afshar, Pedram; Moran, Daniel; Rouse, Adam; Wei, Xuan; Denison, Tim. Validation of chronic implantable neural sensing technology using electrocorticographic (ECoG) based brain machine interfaces; 5th International IEEE/EMBS Conference on Neural Engineering; IEEE; Apr. 2011 p. 704-707.

[4]. Rousche, Patrick J.; Normann, Richard A. Chronic recording capability of the Utah Intracortical Electrode Array in cat sensory cortex. Journal of Neuroscience Methods. Jul; 1998 82(1):1–15. [PubMed: 10223510]

[5]. Bansal, Arjun; Vargas-Irwin, Carlos; Donoghue, John. Relationships among low-frequency local field potentials, spiking activity, and 3-D reach and grasp kinematics in primary motor and ventral premotor cortices. Journal of neurophysiology. Jan; 2011 105(4):1603–1619. [PubMed: 21273313]

[6]. Vargas-Irwin, Carlos E.; Shakhnarovich, Gregory; Yadollahpour, Payman; Mislow, John M K.; Black, Michael J.; Donoghue, John P. Decoding complete reach and grasp actions from local primary motor cortex populations. Journal of neuroscience. Jul; 2010 30(29):9659–69. [PubMed: 20660249]

[7]. Long, John D.; Carmena, Jose M. A statistical description of neural ensemble dynamics. Frontiers in computational neuroscience. Jan.2011 5(52)

[8]. Afshar, Afsheen; Santhanam, Gopal; Yu, Byron M.; Ryu, Stephen I.; Sahani, Maneesh; Shenoy, Krishna V. Single-trial neural correlates of arm movement preparation. Neuron. Aug; 2011 71(3):555–64. [PubMed: 21835350]

[9]. Nicolelis, Miguel A L.; Dimitrov, Dragan; Carmena, Jose M.; Crist, Roy; Lehew, Gary; Kralik, Jerald D.; Wise, Steven P. Chronic, multisite, multielectrode recordings in macaque monkeys; Proceedings of the National Academy of Sciences of the United States of America; Sep. 2003 p. 11041-6.

[10]. Chase, Steven M.; Kass, Robert E.; Schwartz, Andrew B. Behavioral and neural correlates of visuomotor adaptation observed through a brain-computer interface in primary motor cortex. Journal of Neurophysiology. Apr; 2012 108(2):624–644. [PubMed: 22496532]

[11]. Harrison, Reid R.; Kier, Ryan J.; Chestek, Cynthia A.; Gilja, Vikash; Nuyujukian, Paul; Ryu, Stephen; Greger, Bradley; Solzbacher, Florian; Shenoy, Krishna V. Wireless neural recording with single low-power integrated circuit. IEEE transactions on neural systems and rehabilitation engineering. Aug; 2009 17(4):322–9. [PubMed: 19497825]

[12]. Miranda, Henrique; Gilja, Vikash; Chestek, Cindy A.; Shenoy, Krishna V.; Meng, Teresa H. HermesD: A High-Rate Long-Range Wireless Transmission System for Simultaneous Multichannel Neural Recording Applications. IEEE transactions on biomedical circuits and systems. Jun; 2010 4(3):181–191.

[13]. Kipke, Daryle; Williams, Justin; Hetke, Jamille; Henderson, Jaimie; Garell, Charles. US Patent. Intracranial neural interface system. no. 7979105. 2011.

[14]. Song Y-K, Borton David A, Park Sunmee, Patterson William R, Bull Christopher W, Laiwalla Farah, Mislow John, Simeral John D, Donoghue John P, Nurmikko Arto V. Active microelectronic neurosensor arrays for implantable brain communication interfaces. IEEE transactions on neural systems and rehabilitation engineering. Aug; 2009 17(4):339–45. [PubMed: 19502132]

[15]. Borton, David; Yin, Ming; Aceros, Juan; Agha, Naubahar; Minxha, Juri; Komar, Jacob; Patterson, William; Bull, Christopher; Nurmikko, Arto. Developing implantable neuroprosthetics: a new model in pig; 34th Annual International Conference of the IEEE Engineering in Medicine and Biology Society; Jan. 2011 p. 3024-30.

[16]. Nurmikko, Arto V.; Donoghue, John P.; Hochberg, Leigh R.; Patterson, William R.; Song, Yoon-Kyu; Bull, Christopher W.; Borton, David A.; Laiwalla, Farah; Park, Sunmee; Ming, Yin; Aceros, Juan. Listening to Brain Microcircuits for Interfacing With External World-Progress in Wireless Implantable Microelectronic Neuroengineering Devices; Proceedings of the IEEE; Jan. 2010 p. 375-388.

[17]. Rizk, Michael; Obeid, Iyad; Callender, Stephen H.; Wolf, Patrick D. A single-chip signal processing and telemetry engine for an implantable 96-channel neural data acquisition system. Journal of neural engineering. Sep; 2007 4(3):309–21. [PubMed: 17873433]

[18]. Tresco, Patrick A.; Winslow, Brent D. The Challenge of Integrating Devices into the Central Nervous System. Critical Reviews in Biomedical Engineering. Jan; 2011 39(1):29–44. [PubMed: 21488813]

[19]. Simeral, John; Kim, Phil; Black, Michael; Donoghue, John; Hochberg, Leigh. Neural control of cursor trajectory and click by a human with tetraplegia 1000 days after implant of an intracortical microelectrode array. Journal of neural engineering. Apr.2011 8(2):025027. [PubMed: 21436513]

[20]. Hochberg, Leigh R.; Bacher, Daniel; Jarosiewicz, Beata; Masse, Nicolas Y.; Simeral, John D.; Vogel, Joern; Haddadin, Sami; Liu, Jie; Cash, Sydney S.; van der Smagt, Patrick; Donoghue, John P. Reach and grasp by people with tetraplegia using a neurally controlled robotic arm. Nature. May; 2012 485(7398):372–5. [PubMed: 22596161]

[21]. Zerris, Vasilios A.; Donoghue, John D.; Hochberg, Leigh R.; O'Rourke, Daniel Kevin; Chiocca, Ennio Antonio. Braingate: Turning Thought into Action-First Experience with a Human Neuromotor Prosthesis: 885. Neurosurgery. Aug.2005 57(2):425.

[22]. Hochberg, Leigh R.; Serruya, Mijail D.; Friehs, Gerhard M.; Mukand, Jon A.; Saleh, Maryam; Caplan, Abraham H.; Branner, Almut; Chen, David; Penn, Richard D.; Donoghue, John P. Neuronal ensemble control of prosthetic devices by a human with tetraplegia. Nature. Jul; 2006 442(7099):164–71. [PubMed: 16838014]

[23]. Truccolo, Wilson; Donoghue, Jacob A.; Hochberg, Leigh R.; Eskandar, Emad N.; Madsen, Joseph R.; Anderson, William S.; Brown, Emery N.; Halgren, Eric; Cash, Sydney S. Single-neuron dynamics in human focal epilepsy. Nature neuroscience. May; 2011 14(5):635–41.

[24]. Kramer, Mark A.; Cash, Sydney S. Epilepsy as a disorder of cortical network organization. The Neuroscientist. Aug; 2012 18(4):360–72. [PubMed: 22235060]

[25]. Wilson BS, Finley CC, Lawson DT, Wolford RD, Eddington DK, Rabinowitz WM. Better speech recognition with cochlear implants. Nature. Jul; 1991 352(6332):236–8. [PubMed: 1857418]

[26]. Rizk, Michael; Bossetti, Chad A.; Jochum, Thomas A.; Callender, Stephen H.; Nicolelis, Miguel A L.; Turner, Dennis A.; Wolf, Patrick D. A fully implantable 96-channel neural data acquisition system. Journal of neural engineering. Apr.2009 6(2):026002. [PubMed: 19255459]

[27]. Denison, Tim; Consoer, Kelly; Santa, Wesley; Avestruz, Al-Thaddeus; Cooley, John; Kelly, Andy. A 2 W, 100 nV/rtHz Chopper-Stabilized Instrumentation Amplifier for Chronic Measurement of Neural Field Potentials. IEEE journal of solid-state circuits. Dec; 2007 42(12): 2934–2945.

[28]. Denison, Tim; Santa, Wes; Jensen, Randy; Carlson, Dave; Molnar, Gregory; Avestruz, Al-Thaddeus. An 8W Heterodyning Chopper Amplifier for Direct Extraction of 2Vrms Neuronal Biomarkers; IEEE International Solid-State Circuits Conference - Digest of Technical Papers; IEEE; Feb. 2008 p. 162-603.

[29]. Harrison, Reid R.; Charles, Cameron. A low-power low-noise cmos for amplifier neural recording applications. IEEE journal of solid-state circuits. Jun; 2003 38(6):958–965.

[30]. Chestek, Cynthia; Gilja, Vikash; Nuyujukian, Paul; Kier, Ryan J.; Solzbacher, Florian; Ryu, Stephen I.; Harrison, Reid R.; Shenoy, Krishna V. HermesC: low-power wireless neural recording system for freely moving primates. IEEE transactions on neural systems and rehabilitation engineering. Aug; 2009 17(4):330–8. [PubMed: 19497829]

[31]. Patterson, William R.; Song, Yoon-Kyu; Bull, Christopher W.; Ozden, Ilker; Deangellis, Andrew P.; Lay, Christopher; McKay, J Lucas; Nurmikko, Arto V.; Donoghue, John D.; Connors, Barry W. A microelectrode/microelectronic hybrid device for brain implantable neuroprosthesis applications. IEEE transactions on bio-medical engineering. Oct; 2004 51(10):1845–53. [PubMed: 15490832]

[32]. Chae, Moo Sung; Yang, Zhi; Yuce, Mehmet R.; Hoang, Linh; Liu, Wentai. A 128-channel 6 mW wireless neural recording IC with spike feature extraction and UWB transmitter. IEEE transactions on neural systems and rehabilitation engineering. Aug; 2009 17(4):312–21. [PubMed: 19435684]

[33]. Yin, Ming; Ghovanloo, Maysam. Using pulse width modulation for wireless transmission of neural signals in multichannel neural recording systems. IEEE transactions on neural systems and rehabilitation engineering. Aug; 2009 17(4):354–63. [PubMed: 19497823]

[34]. Miranda, Henrique; Meng, Teresa H. A programmable pulse UWB transmitter with 34% energy efficiency for multichannel neuro-recording systems; IEEE Custom Integrated Circuits Conference; IEEE; Sep. 2010 p. 1-4.

[35]. Ghovanloo, Maysam. A clockless ultra low-noise low-power wireless implantable neural recording system; IEEE International Symposium on Circuits and Systems; IEEE; May. 2008 p. 1756-1759.

[36]. Normann, Richard A. A penetrating, cortical electrode array: design considerations; IEEE International Conference on Systems, Man, and Cybernetics; IEEE; 1990. p. 918-920.

[37]. Leuthardt, Eric C.; Schalk, Gerwin; Wolpaw, Jonathan R.; Ojemann, Jeffrey G.; Moran, Daniel W. A brain-computer interface using electrocorticographic signals in humans. Journal of neural engineering. Jun; 2004 1(2):63–71. [PubMed: 15876624]

[38]. Aceros, Juan; Yin, Ming; Borton, David A.; Patterson, William R.; Nurmikko, Arto V. A 32-channel fully implantable wireless neurosensor for simultaneous recording from two cortical regions. Conference proceedings : … Annual International Conference of the IEEE Engineering in Medicine and Biology Society; IEEE Engineering in Medicine and Biology Society. Conference; Jan. 2011 p. 2300-6.

[39]. Bazett H, Love L. Temperature changes in blood flowing in arteries and veins in man. Journal of applied physiology. Jul; 1948 1(1):3–19. [PubMed: 18887571]

[40]. Cooper TE, Trezek GJ. Correlation of thermal properties of some human tissue with water content. Aerospace medicine. Jan; 1971 42(1):24–7. [PubMed: 5541087]

[41]. Pennes HH. Analysis of tissue and arterial blood temperatures in the resting human forearm. Journal of applied physiology. Jul; 1998 85(1):5–34. [PubMed: 9714612]

[42]. Wissler, Eugene. Heat transfer in medicine and biology. Plenum Press; New York, NY: 1985. Mathematical simulation of human thermal behavior using whole body models. chapter 13

[43]. Lind, Nanna Marie; Moustgaard, Anette; Jelsing, Jacob; Vajta, Gabor; Cumming, Paul; Hansen, Axel K. The use of pigs in neuroscience: modeling brain disorders. Neuroscience and biobehavioral reviews. Jan; 2007 31(5):728–51. [PubMed: 17445892]

[44]. Mojarradi, Mohammad; Binkley, David; Blalock, Benjamin; Andersen, Richard; Ulshoefer, Norbert; Johnson, Travis; Del Castillo, Linda. A miniaturized neuroprosthesis suitable for implantation into the brain. IEEE transactions on neural systems and rehabilitation engineering. Mar; 2003 11(1):38–42. [PubMed: 12797724]

[45]. Marcilloux, Jean-Claude; Rampin, Olivier; Felix, Marie-Bernadette; Laplace, Jean-Paul; Fessard, Denise Albe. A stereotaxic apparatus for the study of the central nervous structures in the pig. Brain Research Bulletin. Mar; 1989 22(3):591–597. [PubMed: 2653572]

[46]. Choi, Joon Hwan; Jung, Hae Kyung; Kim, Taejeong. A new action potential detector using the MTEO and its effects on spike sorting systems at low signal-to-noise ratios. IEEE Transactions on Biomedical Engineering. Apr; 2006 53(4):738–746. [PubMed: 16602581]

[47]. Yu, Byron; Cunningham, John P.; Santhanam, Gopal; Ryu, Stephen I.; Shenoy, Krishna V.; Sahani, Maneesh. Gaussian-process factor analysis for low-dimensional single-trial analysis of neural population activity. Journal of neurophysiology. Jul; 2009 102(1):614–35. [PubMed: 19357332]

[48]. Santhanam, Gopal; Yu, Byron M.; Gilja, Vikash; Ryu, Stephen I.; Afshar, Afsheen; Sahani, Maneesh; Shenoy, Krishna V. Factor-analysis methods for higher-performance neural prostheses. Journal of neurophysiology. Aug; 2009 102(2):1315–30. [PubMed: 19297518]

[49]. Yin, Ming; Ghovanloo, Maysam. A low-noise clockless simultaneous 32-channel wireless neural recording system with adjustable resolution. Analog Integrated Circuits and Signal Processing. Nov; 2010 66(3):417–431.

[50]. Szuts, Tobi A.; Fadeyev, Vitaliy; Kachiguine, Sergei; Sher, Alexander; Grivich, Matthew V.; Agrochão, Margarida; Hottowy, Pawel; Dabrowski, Wladyslaw; Lubenov, Evgueniy V.; Siapas, Athanassios G.; Uchida, Naoshige; Litke, Alan M.; Meister, Markus. A wireless multi-channel neural amplifier for freely moving animals. Nature neuroscience. Feb; 2011 14(2):263–9.

[51]. Sodagar AM, Wise KD, Najafi K. A Wireless Implantable Microsystem for Multichannel Neural Recording. IEEE Transactions on Microwave Theory and Techniques. Oct; 2009 57(10):2565–2573.

[52]. Kim, Sung-Phil; Simeral, John D.; Hochberg, Leigh R.; Donoghue, John P.; Friehs, Gerhard M.; Black, Michael J. Multi-state decoding of point-and-click control signals from motor cortical activity in a human with tetraplegia; 3rd International IEEE/EMBS Conference on Neural Engineering; IEEE; May. 2007 p. 486-489.

[53]. Truccolo, Wilson; Friehs, Gerhard M.; Donoghue, John P.; Hochberg, Leigh R. Primary motor cortex tuning to intended movement kinematics in humans with tetraplegia. Journal of neuroscience. Jan; 2008 28(5):1163–78. [PubMed: 18234894]

[54]. Chadwick, Ed; Blana, D.; Simeral, JD.; Lambrecht, J.; Kim, SP.; Cornwell, AS.; Taylor, DM.; Hochberg, LR.; Donoghue, JP.; Kirsch, RF. Continuous neuronal ensemble control of simulated arm reaching by a human with tetraplegia. Journal of neural engineering. Jun.2011 8(3):034003. [PubMed: 21543840]

[55]. Saleh, Maryam; Takahashi, Kazutaka; Hatsopoulos, Nicholas G. Encoding of coordinated reach and grasp trajectories in primary motor cortex. Journal of neuroscience. Jan; 2012 32(4):1220–32. [PubMed: 22279207]

[56]. Tkach, Dennis; Reimer, Jacob; Hatsopoulos, Nicholas G. Congruent activity during action and action observation in motor cortex. Journal of neuroscience. Nov; 2007 27(48):13241–50. [PubMed: 18045918]

[57]. Suner, Selim; Fellows, Matthew R.; Irwin, Carlos Vargas; Nakata, Gordon Kenji; Donoghue, John P. Reliability of signals from a chronically implanted, silicon-based electrode array in non-human primate primary motor cortex. IEEE transactions on neural systems and rehabilitation engineering. Dec; 2005 13(4):524–41. [PubMed: 16425835]

[58]. Achtman, Neil; Afshar, Afsheen; Santhanam, Gopal; Yu, Byron M.; Ryu, Stephen I.; Shenoy, Krishna V. Free-paced high-performance brain-computer interfaces. Journal of neural engineering. Sep; 2007 4(3):336–47. [PubMed: 17873435]

[59]. Ryu, Stephen I.; Shenoy, Krishna V. Human cortical prostheses: lost in translation? Neurosurgical focus. Jul.2009 27(1):E5. [PubMed: 19569893]

[60]. Velliste, Meel; Perel, Sagi; Spalding, M Chance; Whitford, Andrew S.; Schwartz, Andrew B. Cortical control of a prosthetic arm for self-feeding. Nature. Jun; 2008 453(7198):1098–101. [PubMed: 18509337]

[61]. Yin, Ming; Borton, David A.; Aceros, Juan; Patterson, William R.; Nurmikko, Arto V. A 100-channel hermetically sealed implantable device for wireless neurosensing applications; IEEE International Symposium on Circuits and Systems; IEEE; May. 2012 p. 2629-2632.

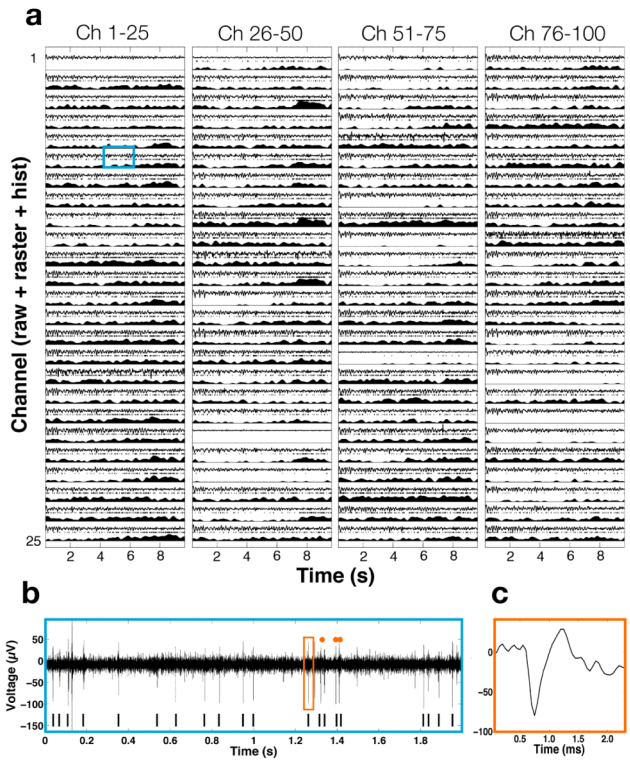

Figure 1.
Wirelessly recorded data from implanted neural interface in non-human primate. Each line (a) contains 10 seconds of unprocessed, raw data (a, top), offline extracted spike raster data (a, middle), and externally computer running firing rate histogram (a, bottom). Channel 6 is expanded (b) to show examples of neural spikes in the data, and further, (c) shows example extracted waveform.

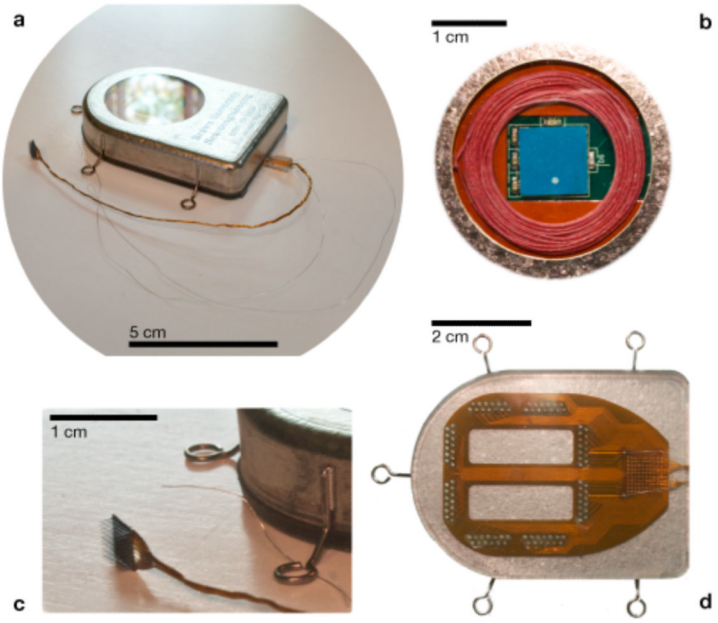

Figure 2.

A wireless neural interface, hermetically sealed, for untethered neuroscience and clinical use. An image of the device after hermetic closure (a) and ready for implant. In a view through the single crystal sapphire window (b), used for electromagnetic transparency, the receiving power coil (red) and the wide band data telemetry chip antenna (blue) can be seen. The intracortical neurosensor, manufactured at Blackrock Microsystems (c), and a reference wire can be seen in relation to the subcutaneous enclosure. Individual wires enter the enclosure through Pt/Ir and ceramic feedthroughs from a flexible polymer (d) interconnect board sealed to the bottom (outside) of the titanium enclosure. The interconnect board is packaged in biocompatible silicone rubber to maintain robust electrical isolation of the input electrodes.

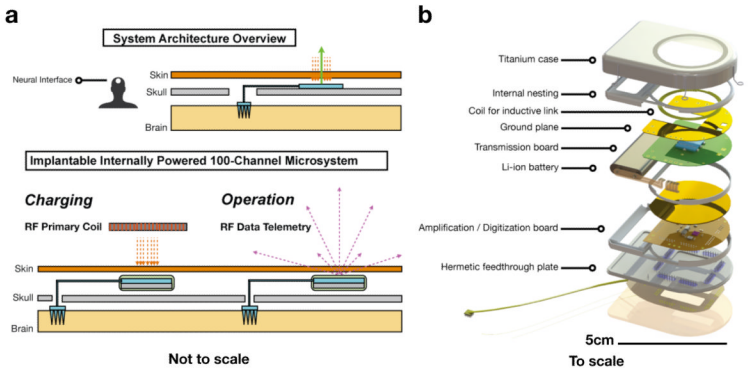

Figure 3.

Architecture, assembly, and functions of a hermetically sealed, wireless, battery powered neural interface. Overview of the wireless neural interface as a subcutaneous implant (not to scale), showing the location of the intracortical microelectrode array and supracranial wireless module (a). The device operates in two modes, battery charging and continuous recording, and is separated into two units, cortical (the commercial MEA) and cranial (the hermetically sealed active electronics). Exploded view (b) of the to scale neurosensor device. The Amplification Board integrates a preamplifier application specific integrated circuit (ASIC) chip, two successive approximation analog-to-digital converters (SAR-ADCs), a controller ASIC, and a 24MHz crystal oscillator (online Methods). The Transmission Board contains a receiving coil for power harvesting: a 27-turn 27mm outer diameter coil made from 46-AWG 40-strand Litz wire for minimum loss.

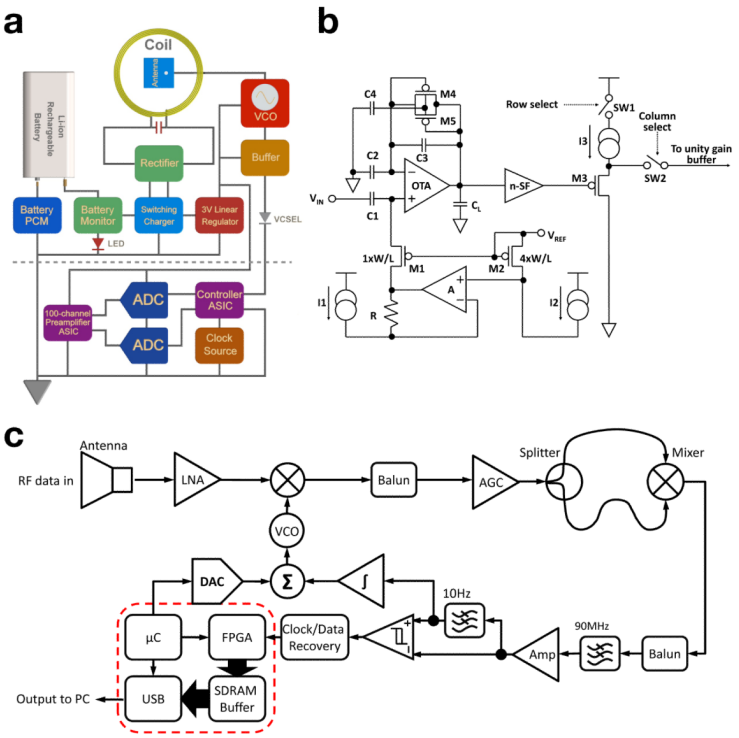

Figure 4.

Electronic schematics of neural interface, amplification circuitry, and telemetry unit. (a) Block diagram of the implantable module, including AB and TxB. The TxB (above the dotted line) receives a TTL input from the AB (below the dotted line) that modulates a freely running commercial VCO. (b) The circuit block diagram of the 100-ch CMOS preamplifier ASIC is shown. The preamplifier uses a capacitive-feedback, folded cascode operational transconductance amplifier (OTA) configuration with a source follower output buffer. (c) The RF superheterodyne receiver (Rx) is shown using a polarized antenna to reduce the sensitivity to movement of the transmitter antenna.

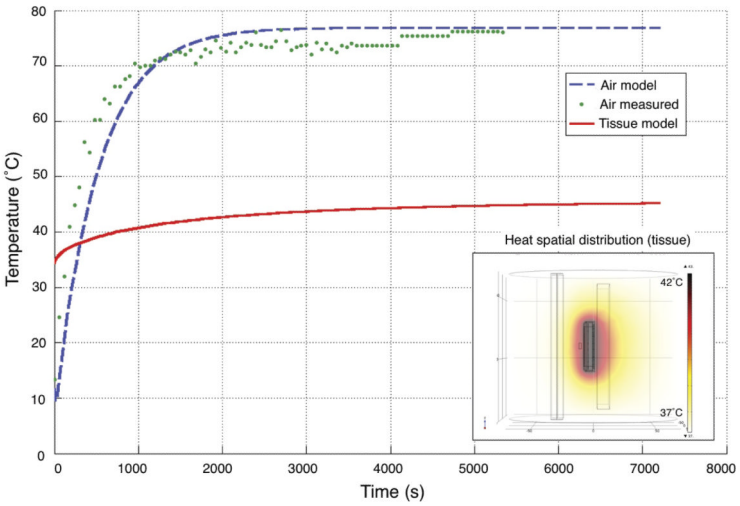

Figure 5.

Temperature vs. time profile of the neural interface during the charging process. The device was charged at a constant 60mA charging current (+30.2mA for the system itself to run), necessitating about 2W of forward powered from the external charger. Experimental temperature measurements in air on benchtop (green, dotted), modeled air calculations (blue, dashed), and modeled calculations of the system in biological tissue (red, solid) are shown in the figure. We operated the neural interface in the first 1000 seconds shown on this plot and applied active cooling to maintain skin temperature at or near 37°*C*.

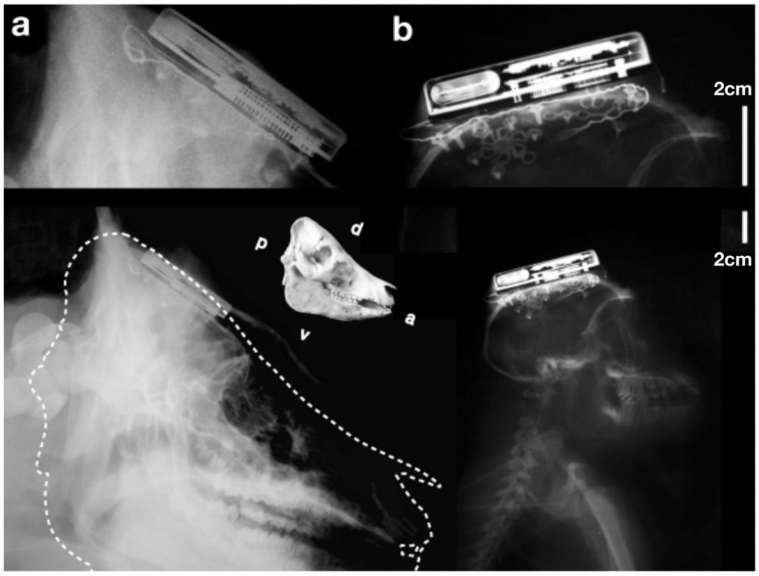

Figure 6.
X-Ray images of implanted neural interface, several months following surgery. Four neural interfaces were implanted in a total of two Yorkshire pigs (a) and two rhesus macaque non-human primates (b). A to-scale skull comparison is shown between animals. In swine, the device can be seen embedded between the cancellous bone and outer table of the cranium. In monkey, X-Ray shows device implanted on outer table of cranium.

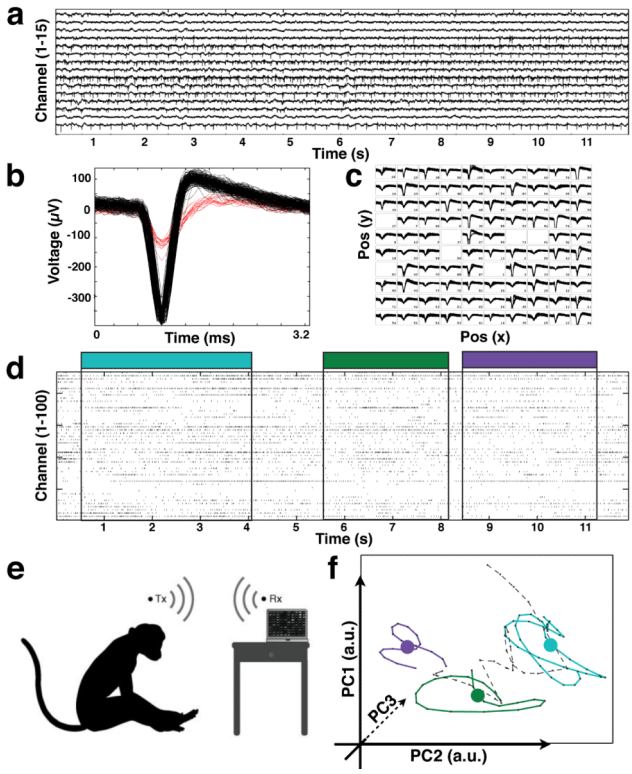

Figure 7.

Wirelessly recorded data from implanted neural interface in non-humanprimates. (a) A selection of 15 of the 100 broadband recording channels richness of high-sample rate (20ksps) data collection. Spikes were extracted (b) on all channels (c) showing single neuron activity on input channels. Raster plot (12s) marking spike timestamps for all input channels is shown with behavior indicated by color overlay. A recording session in primates (e) where subject reaches for food while neural data is recorded wirelessly. Spikes across all channels are reduced to a low-dimensional state space (f) through principal component analysis. We present such neural trajectories produced during free movement of monkey JR: scratching eye (blue), touching an apple (green) and turning head (purple).

Table 1

Current state-of-the-art neural data recording and amplification systems.

Ref	Type	Test model	Noise μV_{rms}	Bit res	S/s ksps	# Ch	Data Mbps	Power mW	Size mm	Tx
Chae [32]	ASIC	Bench	4.9	9	2	128	90	6	8:8 × 7:2×n.r.	UWB
Harrison [11]	ASIC	Bench	5.0	10	15	100	0.35	10	5:4 × 7:0×n.r.	902/928 FSK
Miranda [12]	Device external	NHP 3 mon	5.0	12	30	32	24	142	38 × 38 × 51	3.7/4.1GHz FSK
Yin [49]	Device external	Rat	4.9	8	20	32	2.56	5.6	n.r.×n.r.×n.r.	898/926MHz FSK
Szuts [50]	Device external	Rat 1 hr	3.6	n.r.	20	64	10	645	*n.r.	2.38GHz FM
Sodagar [51]	Device external	Guinea	8.9	8	7.8	64	2	14.4	14 × 16×n.r.	70/200MHz OOK
Rizk [17]	Device external	Rat	n.r.	12	31	96	1	100	50 × 40 × 15	916.5MHz ASK
Rizk [26]	Device implanted	Sheep 3 hr	7	12	31	96	n.r.	2000	50 × 40 × 15	916.5MHz ASK
This work	**Device implanted**	**NHP >13 mon**	**8.6**	**12**	**20**	**100**	**24**	**90.6**	**56×42×11**	**3.2/3.8GHz FSK**

n.r not reported.

* Two-part system, cranial portion + backpack for battery.